Pushing the Limits: 3D Layer-by-Layer-Assembled Composites for Cathodes with 160 C Discharge Rates

Runwei Mo,[†] Siu On Tung,[‡] Zhengyu Lei,[†] Guangyu Zhao,[†] Kening Sun,[*,†] and Nicholas A. Kotov[*,‡]

[†]Academy of Fundamental and Interdisciplinary Sciences, Harbin Institute of Technology, Harbin, 150001, China and [‡]Department of Chemical Engineering, Biointerfaces Institute, University of Michigan, Ann Arbor, Michigan 48109, United States,

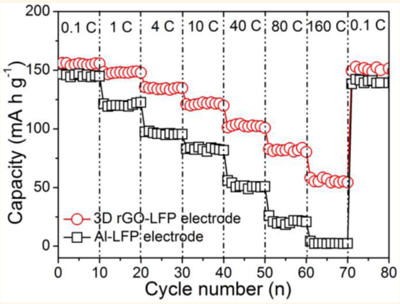

ABSTRACT Deficiencies of cathode materials severely limit cycling performance and discharge rates of Li batteries. The key problem is that cathode materials must combine multiple properties: high lithium ion intercalation capacity, electrical/ionic conductivity, porosity, and mechanical toughness. Some materials revealed promising characteristics in a subset of these properties, but attaining the entire set of often contrarian characteristics requires new methods of materials engineering. In this paper, we report high surface area 3D composite from reduced graphene oxide loaded with $LiFePO_4$ (LFP) nanoparticles made by layer-by-layer assembly (LBL). High electrical conductivity of the LBL composite is combined with high ionic conductivity, toughness, and low impedance. As a result of such materials properties, reversible lithium storage capacity and Coulombic efficiency were as high as 148 mA h g^{-1} and 99%, respectively, after 100 cycles at 1 C. Moreover, these composites enabled unusually high reversible charge–discharge rates up to 160 C with a storage capacity of 56 mA h g^{-1}, exceeding those of known LFP-based cathodes, some of them by several times while retaining high content of active cathode material. The study demonstrates that LBL-assembled composites enable resolution of difficult materials engineering tasks.

KEYWORDS: layer-by-layer assembly · cathodes · cycling performance · graphene · 3D composites · conductive network · lithium ion batteries

The utilization of lithium ion batteries (LIBs) in electric vehicles and a variety of other applications requires marked improvements in charge–discharge (C–D) rates along with energy and power density, safety, and cycle life.[1] It is also important to understand the fundamental limits of battery material performance and the factors controlling them. The C–D rates of LIBs are limited by, among other factors, the rates of ion diffusion through and ion intercalation inside the electrode material.[2–4] They will therefore benefit from shortened diffusion pathways of lithium (and other) ions. Improvement of C–D rates also requires reduction of the tunneling barriers in the conduction pathways for electrons.[5] Porous materials combining both micro- and nanoscale porosity provide the opportunity to engineer both of these pathways.[6,7]

Porous anodes and cathodes with a variety of 3D architectures have been investigated in the past.[8–22] A lot of them exploited the ability of graphene oxide (GO) and graphene (G) to produce voluminous foams with micro-, meso-, and nanoscale pores.[13–18] Other approaches took advantage of pillars from nanoparticles (NPs) or polymers.[19–22] Overall, foamlike composites from G and GO demonstrate improved ion and electron transport. However, two challenges remain. First, 3D composites must have local mechanical properties that allow the pores to withstand continuous expansion–contraction cycles associated with C–D processes. Typically G, GO, and other carbon-based foams have fairly weak interactions between components and display low extensibility,[14–21] which is detrimental to their physical integrity under such conditions. Second, the majority of studies in this area have been focused on anodes, which may not be an ideal approach.[11–13,22] Considering many accounts, the cathodes represent the weakest link for making durable high C–D rate batteries.[23–26] In this respect, the utilization of thin, mesoscale 3D conductive networks, templated by Ni

* E-mail: keningsunhit@126.com, kotov@umich.edu.

Received for review December 16, 2014 and accepted April 24, 2015.

10.1021/nn507186k

TABLE 1. Comparison of the Rate Performance of LFP-Based Composites Prepared by Various Methods

materials	method of preparation	active material (%)	carbon content (%)	binder/carbon black (%/%)	rate (C)	capacity (mAh g^{-1})	reference
C-LFP	carbon from glucose	77.5	2.5	10/10	1	139	36
C-LFP	nanocasting	76.8	3.2	10/10	10	112	37
C-LFP	carbon from PEG	72.8	2.2	5/20	20	96	38
					30	75	
C-LFP	carbon from D-gluconic acid	66.2	3.8	15/15	20	68	39
					30	46	
CNT-LFP	solid state reaction	66	4	15/15	10	82	40
					50	65	
CNT-LFP	hydrothermal process	77.5	2.5	10/10	10	104	41
CNT-LFP	chemical vapor deposition	77	13	10/0	10	101	42
GNs-LFP	mechanical mixing	75	5	5/15	30	94	43
					60	68	
GNs-LFP	solvothermal route	67	13	8/12	20	69	44
					40	42	
GNs-LFP	sol—gel route	73.5	1.5	10/15	10	75	45
					15	60	
LFP	**solid-state reaction**	**30**	**0**	**5/65**	**197**	**125**	46
					397	**62**	
3D LBL rGO composite	+ **route**	**90**	**10**	**0/0**	**40**	**101**	**this work**
					80	**81**	
					160	**56**	

foam,[17,18] appears to be a promising approach for significant improvements in cathode performance because it may not only increase both the rates of ion diffusion and intercalation but also must be accompanied by the optimization of the mechanical, electrical, and other properties of the materials forming the 3D network.

In this work, we decided to address the cathode problems by employing materials engineering of cathode materials using 3D composites formed *via* layer-by-layer (LBL or LbL) assembly. The high electrical conductivity,[31−33] toughness, strength, and extensibility[27−30] known for LBL composites can potentially lead to cathodes with considerably improved C—D rates and cyclability. This technique can be used make conformal coatings on substrates with complex geometries, which opens the possibility of producing multilayer films with highly controlled topology.[34,35] Here we demonstrate that Ni-foam-templated LBL composites can serve as cathode materials that can withstand C—D rates as high as 160 C, which is one of the highest known values (Table 1).[46] Moreover, these composites display excellent cycling performance associated with improved mechanical properties of cathode material.[36−46] In addition to their relevance to the field of energy storage, these findings indicate that LBL composites provide a pathway for the engineering and production of materials with function-oriented combinations of properties exceeding the range of traditional materials.

RESULTS AND DISCUSSION

Among many different materials that can serve as active ion-intercalating materials, lithium ferrous phosphate (LFP) was chosen here for cathodes because of its high theoretical specific capacity of 170 mA h g^{-1}, low toxicity, and low cost.[47−49] Standard LFP cathodes suffer from short cycle lives because of brittleness of the material and loss of physical integrity upon repeated expansion—contraction cycles that occur during the C—D of LIBs.[50−52] We hypothesized that engineering a composite material comprised of reduced graphene oxide (rGO) and LFP using LBL can address this problem and also lead to improved C—D rates. We believe that this process will provide a materials engineering protocol that will allow for the construction of materials that approach the limits of materials performance as it did in several other cases.[53−55] Scheme 1 illustrates the fabrication of the 3D, free-standing LBL composite used in our experiments. We started with GO suspensions, prepared by a standard method.[56,57] The carboxylic groups of GO, GO—COO^-, rendered the prepared sheets negatively charged over a wide range of pH. Following GO exfoliation, we derivatized the sheets with N-ethyl-N′-(3-(dimethylamino)propyl)carbodiimide (EDC)-mediated coupling with ethylenediamine to obtain positively charged sheets, GO—NH_3^+. Dispersions of GO—NH_3^+ and GO—COO^- in water at pH 6 displayed zeta potentials of $\zeta = 37 \pm 13.6$ and -41 ± 10.4 mV, respectively.

The multilayer LBL films were produced by sequential adsorption of GO—COO^- and GO—NH_3^+ onto a macroscopic piece of Ni foam serving as a porous template following the traditional LBL assembly sequence and is similar to the methods of 3D LBL composites that we used in the past with making replicas of colloidal crystals.[58,59] To prepare the free-standing 3D LBL composite, a thin layer of poly(methyl methacrylate) (PMMA, a transparent thermoplastic) was deposited on the surface of the LBL films as a sacrificial support layer to prevent the $(GO-NH_3^+/GO-COO^-)_n$ LBL composite from collapsing during removal of the template. Ni foam was etched away in a 3 M HCl solution at 80 °C (Methods), and the PMMA layer was then removed using an acetone bath (Figure S2). The process resulted in stable 3D LBL composite monoliths (Figure S1c,d). To incorporate LFP into the $(GO-NH_3^+/GO-COO^-)_n$ matrix, we used a solvothermal method of NP synthesis (Methods) that enabled us to make sufficiently small LFP NPs with direct electrical contact between the NPs and the underlying multilayer matrix essential for fast electron transport. After that, the obtained carbon-based LBL composite with LFP was annealed at 600 °C for 3 h in an Ar/H_2 atmosphere in order to completely reduce GO to rGO and improve the crystallinity of the LFP NPs.

After the removal of the Ni template and the PMMA layer, the multilayer composite replicated the porous structure of Ni foam (Figure S1c,d,g) as seen in other examples of 3D LBL films.[60−62] The resulting free-standing 3D LBL composite can be described as network of approximately 60 μm wide struts with pore sizes of 200−400 μm (Figure 1a,b and Figure S1e,f). A strong X-ray diffraction (XRD) peak observed at 10° (pattern I) for $(GO-NH_3^+/GO-COO^-)_n$ is characteristic of GO.[63] This peak disappears after the solvothermal treatment, and a new peak at ∼26° (pattern II) associated with (002) diffraction of rGO emerged,[64,65] indicating the reduction of GO (Figure 1d). It was topologically similar to the 3D graphene network obtained by a ga-phase reaction using methane as a source of carbon[17,18] but without the need for high-vacuum conditions and free from solution-processable GO dispersions. Solution-based LBL processing also enabled engineering of its electrical, and most importantly, mechanical properties. The electrical conductivity of the 3D LBL composite was ∼16 S/cm, which is considerably higher than that of previously reported examples of G/rGO composites,[15,17,66,67] including those grown by CVD.[17] These results are attributed to better sheet-to-sheet connectivity characteristic of LBL (Figure S3) and related reduction of the tunneling barrier for electron transport.[68] A slight decrease of the conductivity for greater n is attributed to the packing imperfections associated with increased layering on highly curved substrates and the relatively large size of rGO sheets (Figure S4). For subsequent studies of the cathode performance of these composites, we used materials with $n = 3$ that display the maximum conductivity and high surface area of 480 $m^2\ g^{-1}$ (Figure S5).

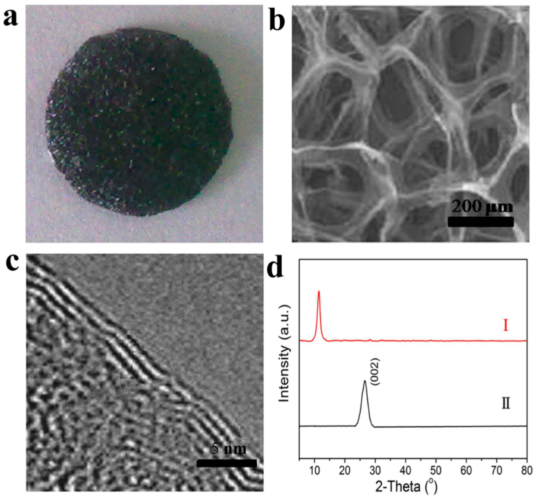

Figure 1. (a) Photograph and (b) SEM image of free-standing 3D LBL composite matrix after removal of Ni foam. (c) TEM image of rGO nanosheets in the composite. (d) XRD patterns of 3D LBL composite (I) before and (II) after the solvothermal treatment.

The interconnected network of the 3D LBL composite provides great potential for the use of this material in LIBs. As an example, we fabricated 3D LBL composites carrying LFP NPs *via* an *in situ* solvothermal synthesis (Figure 2a). No significant deformation of the struts was observed when the composite was loaded with LFP NPs (Figure 2a,b). The diameter of LFP NPs was <100 nm (Figure 2c), which is conducive for fast ion intercalation. The high-resolution TEM

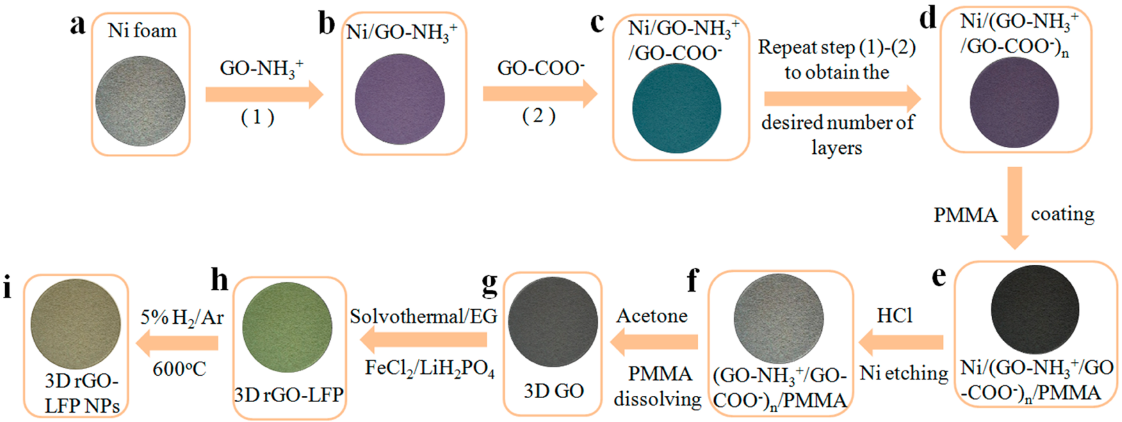

Scheme 1. Preparation of layer-by-layer-assembled 3D rGO-LFP composite.

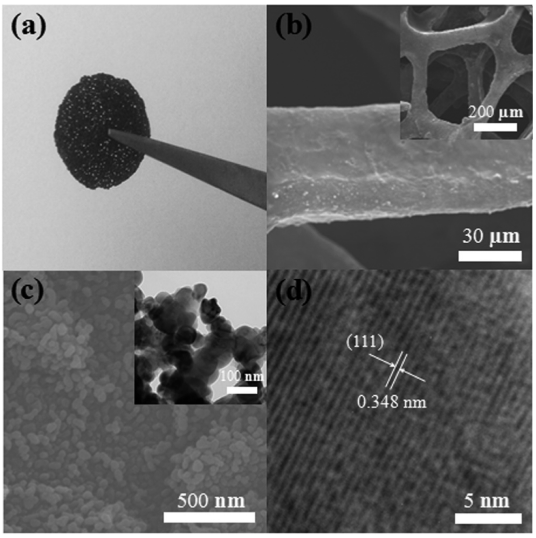

Figure 2. (a) Photograph and (b) SEM image of a free-standing 3D LBL composite loaded with LFP. (c) SEM image of the layer of LFP NPs on the multilayers. The inset in c is a TEM image of LFP NPs on the 3D rGO matrix. (d) HRTEM images of LFP NPs on the 3D rGO matrix.

image of an individual LFP NP displays a crystal lattice with a spacing of 0.348 nm corresponding to the (111) plane (Figure 2d). XRD patterns of LFP prepared by the solvothermal route with and without the multilayer support show well-resolved diffraction peaks indexed to olivine $LiFePO_4$ (PDF 81-1173, International Centre for Diffraction Data, Figure S6). The diffraction peak corresponding to (002) spacing of graphene is eclipsed by the $LiFePO_4$ (111) peak.

In the Raman scattering spectrum, the D peak usually corresponds with the *k*-point phonons of A_{1g} symmetry, whereas the G peak is related to the E_{2g} phonons of C_{sp2} atoms.[70] Their relative intensity gives a clue to the ordered and/or disordered crystal structures of graphene.[69] The Raman scattering spectra of the obtained 3D LBL composites showed a broad D band at 1330 cm^{-1} and a broad G band at 1590 cm^{-1} (Figure S7). It is well-known that the ratio of D band intensity to G band intensity (I_D/I_G) reflects the degree of graphitization for carbonaceous materials and the defect density.[71] The value of I_D/I_G for GO was higher in the 3D LBL composite, indicating a reduction in the average size of the sp_2 domains after GO reduction. In addition, Figure S8 shows the C 1s X-ray photoelectron spectroscopy (XPS) spectra recorded before and after the deposition of LFP NPs. After deconvolution, the C 1s XPS spectrum of the 3D GO LBL composite (Figure S8a) displays the lower binding energy features at 284.5 eV corresponding to C−C carbon and the higher binding energy feature at 288.8 eV, followed by a shoulder at 288.4 eV that is typically assigned to C−OH and C═O from epoxide, hydroxyl, and carboxyl groups. GO was reduced during the synthesis of 3D rGO and 3D rGO-LFP LBL composites; thus, the intensity of XPS peaks from C−OH, C═O, and C−OOH groups decreased greatly compared to those of the 3D GO LBL composite (Figure S8b,c). One can also note that the ratio of the area under peaks corresponding to C−OH, C═O, and C−OOH groups to the area under peaks corresponding to nonoxygenated C of 3D rGO (0.14) is lower than that of 3D rGO-LFP LBL composite (0.16). Moreover, one can identify the appearance of an additional peak at 288.6 eV compared to the version of this composite without LFP NPs. Considering that (1) the peaks for all oxidation states of carbon moved to lower values of binding energies and (2) C═O groups are completely reduced in an earlier step of the process (Figure S8b) this new band cannot be attributed to carboxyl groups. Instead, this 288.6 eV peak should arise from the electronic states of carbon atoms interacting with phosphate groups of the LFP surface. These XPS data indicate that there is an atomic level connectivity between the structural (composite) and active (LFP) components of the cathode material.

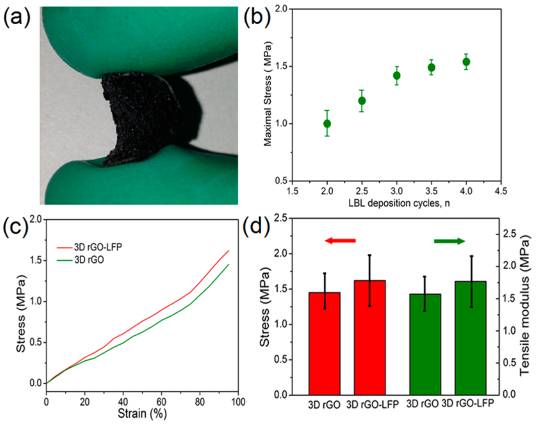

Figure 3. (a) Photograph of 3D LBL composites showing its flexibility. (b) Maximal stress of 3D LBL composite as a function of the number of LBL deposition cycles, *n*. (c) Typical stress−strain curves of free-standing 3D LBL composite with and without LFP NPs. (d) Tensile strength and modulus of 3D LBL composite with and without LFP NPs.

All LBL composites were very flexible and bent without breaking (Figure 3a). They also displayed extensibility with and without LFP NPs exceeding 90%. This is at least one order of magnitude greater than that of the typical LFP-based or other layered composites without the 3D architecture and essential for electrode materials that have to undergo high strains during the lithiation−delithiation process.[72] The maximal stress that they can sustain reached a plateau of 1.45 MPa for *n* = 3 and increased slightly after the deposition of LFP NPs (Figure 3c,d). In addition, the toughness of the 3D LBL composites is 69.9 MJ/m^3, calculated by using the integral under the strain−stress curve.

This set of electrical and mechanical properties makes the composites promising candidates for applications in LIBs. We investigated electrochemical properties of 3D LBL composite composites with *n* = 3 as a cathode material for LIBs. For comparative purposes, we also provide data for cathodes made by drop-casting

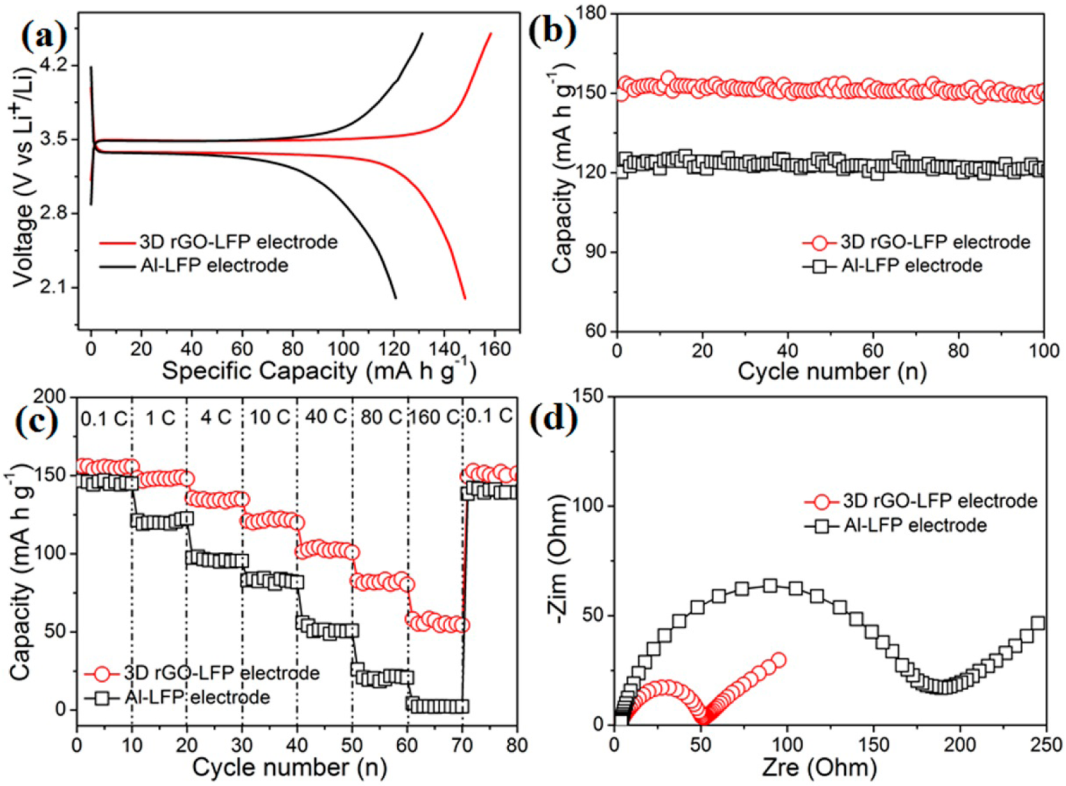

Figure 4. (a) First-cycle discharge curves of the free-standing 3D LBL composite and Al-LFP electrodes. (b) Cycling performance of the electrodes: free-standing 3D LBL composite and Al-LFP. The electrodes were charged−discharged between 2.0 and 4.5 V (vs Li/Li$^+$) at a rate of 170 mA g^{-1} (1 C). (c) Rate-performance of the free-standing 3D LBL composite and Al-LFP electrodes. (d) Nyquist plots of the free-standing 3D LBL composite and Al-LFP electrodes.

LFP slurry onto an aluminum foil that is commonly used in lithium ion batteries.[73] The total loading of LFP for the 3D LBL composite and Al foil was ∼5.4 mg. Because of its relatively high electrical conductivity of ∼16 S/cm, our composite also served as the current collector, which is important for reducing the weight of the battery. The initial specific discharge capacity observed for the 3D LBL composite electrode at 1 C rate (170 mA g^{-1}) was 149 mA h g^{-1}. This is considerably higher than that of an Al-LFP electrode, 121 mA h g^{-1}. We attribute this increase to the efficient charge transport to and from all LFP NPs from the composite matrix and significant reduction of contact resistance enabled by the atomic-level connectivity between the rGO sheets and LFP NPs. This conclusion can be confirmed by comparing cyclic voltametry (CV) patterns of the 3D LBL composite electrode and the Al-LFP electrode. Both electrodes displayed a redox wave at 3.58/3.28 V (scan rate = 0.1 mV s^{-1}), typical for Fe^{2+} /Fe^{3+} at and consistent with a two-phase redox reaction of $LiFePO_4 \rightarrow FePO_4 + Li^+ + e^-$ (Figure S9). Besides greater current density, the peak separation observed for the 3D composite electrode is about 40 mV smaller than that exhibited by the Al-LFP electrode. This result is indicative of the faster kinetics of electron transfer for the 3D LBL composite electrode than for traditional Al-LFP electrodes.

A stable capacity was reached after a few C−D cycles (Figure 4b). Importantly, no detectable decline in capacity was observed after 100 cycles. At that point, the 3D LBL composite electrode displayed a capacity of 148 mAh g^{-1} at the same 1 C discharge rate, corresponding to a Coulombic efficiency of 99% (Figure S10). This result is indicative of the excellent cyclability of the prepared cathodes as well as electrochemical stability and reversibility of the 3D LBL composite electrode (Figure S11).

C−D experiments demonstrated that the 3D LBL composite electrode can sustain unusually high C−D rates (Figure 4). The voltage profiles of the 3D LBL composite electrode for charging to 4.5 V and discharging to 2 V at increasing rates ranging from 0.1 to 160 C are shown in Figure S12a. As expected, the charge capacity and the discharge capacity exhibit a tendency to decrease with increasing current density. For example, the characteristic discharge plateau around 3.42 V at 0.1 C drops to about 3.06 V at 160 C. The presence of the plateau region at 3.42−3.06 V indicates that the intercalation of Li$^+$ ion does indeed take place.

Figure 4c compares the C−D rate performance of the 3D LBL composite electrode with an Al-LFP electrode. The reversible capacity of the 3D LBL composite electrode was initially stabilized at 155 mA h g^{-1} after 10 cycles at a rate of 0.1 C. We then gradually increased

C−D rates to 1, 4, 10, 40, 80, and 160 C; the corresponding reversible capacities were 146, 135, 121, 103, 81, and 56 mA h g^{-1}. This electrode performance can be compared to the reversible capacity of Al-LFP electrodes that was found to be 144, 121, 97, 82, 51, 21, and 2 mA h g^{-1} for the C−D rates of 0.1, 1, 4, 10, 40, 80, and 160 C, respectively (Figure 4). Importantly, the original capacity at 0.1 C is reversible after cycling at high rates, including 160 C. The capacity decreases to less than 2% of the initial value after 100 cycles, indicating that 3D LBL composite retains its physical integrity even under such extreme electrochemical conditions (Figure S12b). Importantly, high C−D rate capacity is also accompanied by high cyclability and an overall increase in capacity compared to those of LFP-based electrodes made by other techniques including those made from other carbon-based foams (Table 1). In this respect, it is meaningful to compare the performance of LBL-made cathodes with those reported by Kang and Ceder.[46] The extremely high rates of charge and discharge of 197 and 397 C were successfully obtained by these researchers for electrodes that contained 30 wt % active material, 65 wt % carbon, and 5 wt % binder. The highest rates (397 C) could only be observed for a cathode composition with a large amount of carbon, which reduces the volumetric and mass energy density of the electrode. In our case, 160 C C−D rates were obtained for our electrodes with 90 wt % active material and 10 wt % carbon.

Capacity per unit mass of the electrodes based on LBL composite was better than that for the Al-LFP electrode, owing to the lightweight mass of the rGO-based composite (∼0.6 mg). The abilities of LBL-made materials to (1) provide high conductivity and (2) minimize the need for conductive additives and binding agents are significant in this perspective. If we include the mass of the entire electrode comprised of electrochemically active material, additives, and conductive substrate, then the maximum specific capacity of the 3D LBL composite is 135 mAh g^{-1}, which is 245% higher than that of the Al-electrode (Figure S13).

Comparative evaluation of electrochemical impedance spectroscopy (EIS) data with respect to the "flat" LFP-based electrodes can help to better understand the origin of the unusually high rate performance of the prepared cathode materials. We obtained EIS curves after the 10th cycle at a C−D rate of 0.1 C (Figure 4d). The semicircle in the Nyquist plot is characteristic of the sum of contact, i.e., the solid−electrolyte interphase, and charge-transfer resistance, whereas the subsequent line inclined at an approximately 45° angle to the real axis characterizes the lithium-diffusion process within the electrodes. The equivalent circuit fitting of EIS spectra using R_s (solution resistance), R_f (contact resistance), and R_{ct} (charge-transfer resistance, Figure S14 and Table S1) indicate that R_f and R_{ct} values of the 3D LBL composite electrode are smaller than those of standard LFP electrodes. Reduction of surface resistance and R_{ct} for 3D LBL is attributed to optimized connectivity of rGO nanosheets in the LBL-assembled composite while enabling fast ion transport for lithium ions because of the microscale porosity. Close contact of LFP NPs with the rGO sheets also accelerates electron transport through the cathode material.

CONCLUSIONS

The high cycling performance of the LBL composites is attributed to their improved mechanical integrity, extensibility, and toughness, which help the material withstand the large mechanical deformations associated with expansion and contraction of electrode material. Although the C−D rates achieved in this work are unlikely to be feasible for use in actual batteries in the near future because of safety concerns and the necessity of optimizing all other battery components, this study shows that such rapid C−D rates for electrodes with a high amount of active material are fundamentally possible. Materials engineering of the ion-conducting membranes using novel nanoscale components that can reduce dendrite growth[74] and low impedance anodes with surface area current collectors[75] may lead to the feasible ultrahigh C−D rate batteries that can reach their full capacity within minutes.

METHODS

Synthesis of Graphene Oxide. GO was prepared from graphite flakes by a modified version of Hummers method.[52,56] Briefly, 1.0 g of graphite flakes, 1.0 g of $NaNO_3$, and 46 mL of concentrated H_2SO_4 were mixed together in an ice bath for 4 h. A 6.0 g portion of $KMnO_4$ was then added slowly into the solution. Afterward, the ice bath was removed, and the suspension was stirred for another 4 days at room temperature. The suspension was then treated with 200 mL of warm water (∼60 °C) and 10 mL of H_2O_2 (30%). The mixture was centrifuged at 4000 rpm and washed with dilute HCl and water until neutral, providing a homogeneous GO aqueous dispersion (1 mg mL^{-1}) suitable for further use.

LBL Assembly. The concentration of GO solutions used in all of the deposition experiments was fixed at 0.10 wt %. The $(GO{-}NH_3^+/GO{-}COO^-)_n$ multilayer-coated Ni templates were prepared using a previously described procedure.[30] In brief, 100 μL of a concentrated dispersion (6.4 wt %) of negatively charged Ni template was diluted to 1 mL with deionized water. Subsequently, 1 mL of $GO{-}NH_3^+$ was added. After deposition for 15 min with a gentle vortex, the excess $GO{-}NH_3^+$ was removed by three centrifugation (9000 rpm for 8 min) wash cycles. A suspension of $GO{-}COO^-$ was then allowed to deposit onto the $GO{-}NH_3^+$-coated Ni foam under the same conditions. The above process was repeated until three layers of $(GO{-}NH_3^+/GO{-}COO^-)_3$ had been deposited onto the Ni foam.

To prevent structural failure of the LBL-made composite trusses under capillary tension when the nickel was etched away, a thin PMMA layer was used as a support to reinforce the GO structure. The Ni foam covered with GO was drop-coated with a PMMA solution and then baked at 160 °C for 40 min. This process solidified the PMMA to form a thin film on the GO surface (Ni-GO-PMMA). Then, the samples were put into an HCl (3 M) solution at 80 °C for 5 h to dissolve the nickel. Finally, a free-standing composite replica of the foam was obtained by dissolving the PMMA with hot acetone at 60 °C.

Solvothermal Synthesis of LPF NPs on 3D LBL Composite. A $FeCl_2 \cdot 4H_2O/LiH_2PO_4$ mixture with a molar ratio of 1:1.1 was dissolved in 70 mLof ethylene glycol, and 35 μL of hydrazine was added after ultrasonic dispersion while stirring constantly for 1 h under nitrogen atmosphere. Subsequently, a piece of 3D composite foam was soaked in this solution before being transferred to a 100 mL Teflon-lined autoclave. The autoclave was sealed, kept at 200 °C for 12 h, and then cooled to room temperature. The 3D composite was washed with deionized water and dried in an oven at 80 °C. Finally, the as-prepared sample was heated at 600 °C for 3 h under a hydrogen/argon (5:95 v/v) atmosphere. LFP NPs can also prepared by a similar procedure without a substrate.

Material Characterization. XRD was carried out with monochromated Cu Kα radiation at a scanning rate of 2° min^{-1} in the range of 5−80° on a Rigaku D/max-γB apparatus. Zeta-potential measurements were obtained by using an electrophoretic light scattering and dynamic light scattering spectrophotometer (DelsaNano C). The morphology of the products was characterized by SEM (using a Hitachi S4800 apparatus) and high-resolution TEM (HRTEM, using a JEM-2100 apparatus) with an accelerating voltage of 200 kV. The strength of the composite was measured with a high-precision mechanical testing system (Instron 5500R materials tester). The surface area was measured by the Brunauer−Emmett−Teller method using ASAP2020. Additionally, Raman spectra were recorded at room temperature by employing an InVia Raman spectrometer using a 633 nm red laser with 10% intensity to determine the extent of graphitic disorder. XPS experiments were performed on a ULVAC PHI Quantera microprobe.

Carbon content was determined using Vario EL cube (Elementar, Germany). The rGO content in the 3D LBL composite was estimated to be ~10 wt %.

Electrochemical Measurements. For half-cell tests of free-standing 3D LBL composites, coin cells were fabricated. In both cases, a lithium metal foil was used as the counter electrode, 1 M $LiPF_6$ in ethylene carbonate and dimethyl carbonate (1:1, v/v) as electrolyte, and porous polypropylene film as separator. The C−D cycles were performed at different rates at room temperature. The discharge−charge tests were conducted at various rates within a voltage window from 2.0 to 4.5 V (vs Li^+/Li) on the BTS battery testing system (Neware, Shenzhen, China).

The loading of LFP on both the 3D LBL composite and Al foil was 5.4 mg. The Al-LFP electrode was prepared by mixing the neat LFP powder, carbon black (Super-P), and polyvinyldifluoride (PVDF, Kynar HSV 900) at a weight ratio of 75:15:10 in *N*-methylpyrrolidone (NMP) to make a slurry. The mixture was pasted onto aluminum foil and then pressed and dried under vacuum at 120 °C for 12 h. Battery cells were assembled in an argon-filled glovebox with oxygen and water content below 1 and 0.1 ppm, respectively.

The electrical conductivity of composite was measured by a standard four-point probe configuration using an electrically conducting silver epoxy (EPO-TEK H20E, Epoxy Technology, Inc.).

CV was performed on an electrochemical workstation (CHI, 660 d) between 2.6 and 4.5 V at a scan rate of 0.1 mV s^{-1}. EIS experiments were carried out on a Parstat 2273 Advanced Electrochemical Systems apparatus primarily in the frequency range from 100 kHz to 10 mHz with the ac signal amplitude of 5 mV.

Conflict of Interest: The authors declare the following competing financial interest(s): N.A.K. declares contractual obligations to Samsung Technologies and being a founder of Elegus Technologies.

Acknowledgment. We thank the Harbin Institute of Technology and the Natural Science Foundation of China (21076023) for the primary financial support of this work. Our work was also sponsored by the Samsung Global Research Outreach (GRO) program and NSF grant no. 1240264 EFRI-ODISSEI.

Supporting Information Available: Additional experimental details and characterization data as described in the text. The Supporting Information is available free of charge on the ACS Publications website at DOI: 10.1021/nn507186k.

REFERENCES AND NOTES

1. Guo, Y. G.; Hu, J. S.; Wan, L. J. Nanostructured Materials for Electrochemical Energy Conversion and Storage Devices. *Adv. Mater.* **2008**, *20*, 2878–2887.
2. Guo, Y. G.; Hu, Y. S.; Sigle, W.; Maier, J. Superior Electrode Performance of Nanostructured Mesoporous TiO_2 (Anatase) through Efficient Hierarchical Mixed Conducting Networks. *Adv. Mater.* **2007**, *19*, 2087–2091.
3. Hu, Y. S.; Guo, Y. G.; Dominko, R.; Gaberscek, M.; Jamnik, J.; Maier, J. Improved Electrode Performance of Porous $LiFePO_4$ Using RuO_2 as an Oxidic Nanoscale Interconnect. *Adv. Mater.* **2007**, *19*, 1963–1966.
4. Wang, Y.; Cao, G. Developments in Nanostructured Cathode Materials for High-Performance Lithium-Ion Batteries. *Adv. Mater.* **2008**, *20*, 2251–2269.
5. Kim, J. Y.; Kotov, N. A. Charge Transport Dilemma of Solution-Processed Nanomaterials. *Chem. Mater.* **2014**, *26*, 134–152.
6. Long, J. W.; Dunn, B.; Rolison, D. R.; White, H. S. Three-Dimensional Battery Architectures. *Chem. Rev.* **2004**, *104*, 4463–4492.
7. Rolison, D. R.; Long, R. W.; Lytle, J. C.; Fischer, A. E.; Rhodes, C. P.; McEvoy, T. M.; Bourga, M. E.; Lubers, A. M. Multifunctional 3D Nanoarchitectures for Energy Storage and Conversion. *Chem. Soc. Rev.* **2009**, *38*, 226–252.
8. Zhang, H. G.; Yu, X. D.; Braun, P. V. Three-Dimensional Bicontinuous Ultrafast-Charge and -Discharge Bulk Battery Electrodes. *Nat. Nanotechnol.* **2011**, *6*, 277–281.
9. Ergang, N. S.; Lytle, J. C.; Lee, K. T.; Oh, S. M.; Smyrl, W. H.; Stein, A. Photonic Crystal Structures as a Basis for a Three-Dimensionally Interpenetrating Electrochemical-Cell System. *Adv. Mater.* **2006**, *18*, 1750–1753.
10. Gerasopoulos, K.; Pomerantseva, E.; McCarthy, M.; Brown, A.; Wang, C. S.; Culver, J.; Ghodssi, R. Hierarchical Three-Dimensional Microbattery Electrodes Combining Bottom-Up Self-Assembly and Top-Down Micromachining. *ACS Nano* **2012**, *6*, 6422–6432.
11. Liu, B. R.; Soares, P.; Checkles, C.; Zhao, Y.; Yu, G. H. Three-Dimensional Hierarchical Ternary Nanostructures for High-Performance Li-Ion Battery Anodes. *Nano Lett.* **2013**, *13*, 3414–3419.
12. Yu, Y.; Yan, C. L.; Gu, L.; Lang, X. Y.; Tang, K.; Zhang, L.; Hou, Y.; Wang, Z. F.; Chen, M. W.; Schmidt, O. G.; Maier, J. Three-Dimensional (3D) Bicontinuous Au/Amorphous-Ge Thin Films as Fast and High-Capacity Anodes for Lithium-Ion Batteries. *Adv. Energy Mater.* **2013**, *3*, 281–285.
13. Chang, Y. H.; Li, J.; Wang, B.; Luo, H.; He, H. Y.; Song, Q.; Zhi, L. J. Synthesis of 3D Nitrogen-Doped Graphene/Fe_3O_4 by a Metal Ion Induced Self-Assembly Process for High-Performance Li-ion Batteries. *J. Mater. Chem. A* **2013**, *1*, 14658–14665.
14. Choi, B. G.; Yang, M. H.; Hong, W. H.; Choi, J. W.; Huh, Y. S. 3D Macroporous Graphene Frameworks for Supercapacitors with High Energy and Power Densities. *ACS Nano* **2012**, *6*, 4020–4028.
15. Chen, W. F.; Li, S. R.; Chen, C. H.; Yan, L. F. Self-Assembly and Embedding of Nanoparticles by *In Situ* Reduced Graphene for Preparation of a 3D Graphene/Nanoparticle Aerogel. *Adv. Mater.* **2011**, *23*, 5679–5683.
16. Lee, J. H.; Park, N.; Kim, B. G.; Jung, D. S.; Im, K.; Hur, J.; Choi, J. W. Restacking-Inhibited 3D Reduced Graphene Oxide for High Performance Supercapacitor Electrodes. *ACS Nano* **2013**, *7*, 9366–9374.

17. Chen, Z. P.; Ren, W. C.; Gao, L. B.; Liu, B. L.; Pei, S. F.; Cheng, H. M. Three-dimensional Flexible and Conductive Interconnected Graphene Networks Grown by Chemical Vapour Deposition. *Nat. Mater.* **2011**, *10*, 424–428.
18. Ji, H. X.; Zhang, L. L.; Pettes, M. T.; Li, H. F.; Chen, S. S.; Shi, L.; Piner, R.; Ruoff, R. S. Ultrathin Graphite Foam: A Three-Dimensional Conductive Network for Battery Electrodes. *Nano Lett.* **2012**, *12*, 2446–2451.
19. Lee, J. M.; Choung, J. W.; Yi, J.; Lee, D. H.; Samal, M.; Yi, D. K.; Lee, C. H.; Yi, G. C.; Paik, U.; Rogers, J. A.; Park, W. I. Vertical Pillar-Superlattice Array and Graphene Hybrid Light Emitting Diodes. *Nano Lett.* **2010**, *10*, 2783–2788.
20. Zhang, L. L.; Xiong, Z. G.; Zhao, X. S. Pillaring Chemically Exfoliated Graphene Oxide with Carbon Nanotubes for Photocatalytic Degradation of Dyes under Visible Light Irradiation. *ACS Nano* **2010**, *4*, 7030–7036.
21. Guo, F.; Creighton, M.; Chen, Y. T.; Hurt, R.; Kulaots, I. Porous Structures in Stacked, Crumpled and Pillared Graphene-based 3D Materials. *Carbon* **2014**, *66*, 476–484.
22. Du, F.; Yu, D. S.; Dai, L. M.; Ganguli, S.; Varshney, V.; Roy, A. K. Preparation of Tunable 3D Pillared Carbon NanotubeGraphene Networks for High-Performance Capacitance. *Chem. Mater.* **2011**, *23*, 4810–4816.
23. Zhao, Y.; Peng, L. L.; Liu, B. R.; Yu, G. H. Single-Crystalline $\mathrm{LiFePO_4}$ Nanosheets for High-Rate Li-Ion Batteries. *Nano Lett.* **2014**, *14*, 2849–2853.
24. Oh, S.-M.; Myung, S.-T.; Park, J. B.; Scrosati, B.; Amine, K.; Sun, Y.-K. Double-Structured $\mathrm{LiMn_{0.85}Fe_{0.15}PO_4}$ Coordinated with $\mathrm{LiFePO_4}$ for Rechargeable Lithium Batteries. *Angew. Chem., Int. Ed.* **2012**, *51*, 1853–1856.
25. Zhang, X. D.; Bi, Z. Y.; He, W.; Yang, G.; Liu, H.; Yue, Y. Z. Fabricating High-Energy Quantum Dots in Ultra-Thin $\mathrm{LiFePO_4}$ Nanosheets Using a Multifunctional High-Energy Biomolecule-ATP. *Energy Environ. Sci.* **2014**, *7*, 2285.
26. Wang, L.; He, X. M.; Sun, W. T.; Wang, J. L.; Li, Y. D.; Fan, S. S. Crystal Orientation Tuning of $\mathrm{LiFePO_4}$ Nanoplates for High Rate Lithium Battery Cathode Materials. *Nano Lett.* **2012**, *12*, 5632–5636.
27. Podsiadlo, P.; Tang, Z. Y.; Shim, B. S.; Kotov, N. A. Counterintuitive Effect of Molecular Strength and Role of Molecular Rigidity on Mechanical Properties of Layer-by-Layer Assembled Nanocomposites. *Nano Lett.* **2007**, *7*, 1224–1231.
28. Lu, C. H.; Donch, I.; Nolte, M.; Fery, A. Au Nanoparticle-based Multilayer Ultrathin Films with Covalently Linked Nanostructures: Spraying Layer-by-layer Assembly and Mechanical Property Characterization. *Chem. Mater.* **2006**, *18*, 6204–6210.
29. Shim, B. S.; Zhu, J.; Jan, E.; Critchley, K.; Kotov, N. A. Transparent Conductors from Layer-by-Layer Assembled SWNT Films: Importance of Mechanical Properties and a New Figure of Merit. *ACS Nano* **2010**, *4*, 3725–3734.
30. Hong, J.; Char, K.; Kim, B. S. Hollow Capsules of Reduced Graphene Oxide Nanosheets Assembled on a Sacrificial Colloidal Particle. *J. Phys. Chem. Lett.* **2010**, *1*, 3442–3445.
31. Hyder, M. N.; Gallant, B. M.; Shah, N. J.; Horn, Y. S.; Hammond, P. T. Synthesis of Highly Stable Sub-8 nm $\mathrm{TiO_2}$ Nanoparticles and Their Multilayer Electrodes of $\mathrm{TiO_2}$/MWNT for Electrochemical Applications. *Nano Lett.* **2013**, *13*, 4610–4619.
32. Hyder, M. N.; Lee, S. W.; Cebeci, F. C.; Schmidt, D. J.; Horn, Y. S.; Hammond, P. T. Layer-by-Layer Assembled Polyaniline Nanofiber/Multiwall Carbon Nanotube Thin Film Electrodes for High-Power and High-Energy Storage Applications. *ACS Nano* **2011**, *5*, 8552–8561.
33. Zhu, J.; Zhang, H. N.; Kotov, N. A. Thermodynamic and Structural Insights into Nanocomposites Engineering by Comparing Two Materials Assembly Techniques for Graphene. *ACS Nano* **2013**, *7*, 4818–4829.
34. Xia, F. F.; Hu, X. L.; Sun, Y. M.; Luo, W.; Huang, Y. H. Layer-by-layer Assembled $\mathrm{MoO_2}$-graphene Thin Film as a High-Capacity and Binder-Free Anode for Lithium-Ion Batteries. *Nanoscale* **2012**, *4*, 4707–4711.
35. Lee, S. W.; Gallant, B. M.; Byon, H. R.; Hammond, P. T.; Horn, Y. S. Nanostructured Carbon-based Electrodes: Bridging the Gap Between Thin-Film Lithium-Ion Batteries and Electrochemical Capacitors. *Energy Environ. Sci.* **2011**, *4*, 1972–1985.
36. Miao, C.; Bai, P. F.; Jiang, Q. Q.; Sun, S. Q.; Wang, X. Y. A Novel Synthesis and Characterization of $\mathrm{LiFePO_4}$ and $\mathrm{LiFePO_4}$/C as a Cathode Material for Lithium-Ion Battery. *J. Power Sources* **2014**, *246*, 232–238.
37. Wang, G. X.; Liu, H.; Liu, J.; Qiao, S. Z.; Lu, G. Q.; Munroe, P.; Ahn, H. Mesoporous $\mathrm{LiFePO_4}$/C Nanocomposite Cathode Materials for High Power Lithium Ion Batteries with Superior Performance. *Adv. Mater.* **2010**, *22*, 4944–4948.
38. Lou, X. M.; Zhang, Y. X. Synthesis of $\mathrm{LiFePO_4}$/C Cathode Materials with Both High-Rate Capability and High Tap Density for Lithium-ion Batteries. *J. Mater. Chem.* **2011**, *21*, 4156–4160.
39. Saravanan, K.; Balaya, P.; Reddy, M. V.; Chowdari, B. V. R.; Vittal, J. J. Morphology Controlled Synthesis of $\mathrm{LiFePO_4}$/C Nanoplates for Li-ion Batteries. *Energy Environ. Sci.* **2010**, *3*, 457–464.
40. Yang, J. L.; Wang, J. J.; Tang, Y. J.; Wang, D. N.; Xiao, B. W.; Li, X. F.; Li, R. Y.; Liang, G. X.; Sham, T.-K.; Sun, X. L. *In Situ* Self-Catalyzed Formation of Core-Shell $\mathrm{LiFePO_4}$@CNT Nanowires for High Rate Performance Lithium-Ion Batteries. *J. Mater. Chem. A* **2013**, *1*, 7306–7311.
41. Chen, M.; Du, C. Y.; Song, B.; Xiong, K.; Yin, G. P.; Zuo, P. J.; Cheng, X. Q. High-performance $\mathrm{LiFePO_4}$ Cathode Material from $\mathrm{FePO_4}$ Microspheres with Carbon Nanotube Networks Embedded for Lithium Ion Batteries. *J. Power Sources* **2013**, *223*, 100–106.
42. Sun, X. R.; Li, J. J.; Shi, C. S.; Wang, Z. Y.; Liu, E. Z.; He, C. N.; Du, X. W.; Zhao, N. Q. Enhanced Electrochemical Performance of $\mathrm{LiFePO_4}$ Cathode with *In-Situ* Chemical Vapor Deposition Synthesized Carbon Nanotubes as Conductor. *J. Power Sources* **2012**, *220*, 264–268.
43. Zhou, X. F.; Wang, F.; Zhu, Y. M.; Liu, Z. P. Graphene Modified $\mathrm{LiFePO_4}$ Cathode Materials for High Power Lithium Ion Batteries. *J. Mater. Chem.* **2011**, *21*, 3353–3358.
44. Zhang, Y.; Wang, W. C.; Li, P. H.; Fu, Y. B.; Ma, X. H. A Simple Solvothermal Route to Synthesize Graphene-modified $\mathrm{LiFePO_4}$ Cathode for High Power Lithium Ion Batteries. *J. Power Sources* **2012**, *210*, 47–53.
45. Yang, J. L.; Wang, J. J.; Tang, Y. J.; Wang, D. N.; Li, X. F.; Hu, Y. H.; Li, R. Y.; Liang, G. X.; Sham, T.-K.; Sun, X. L. $\mathrm{LiFePO_4}$-graphene as a Superior Cathode Material for Rechargeable Lithium Batteries: Impact of Stacked Graphene and Unfolded Graphene. *Energy Environ. Sci.* **2013**, *6*, 1521–1528.
46. Kang, B. W.; Ceder, G. Battery Materials for Ultrafast Charging and Discharging. *Nature* **2009**, *458*, 190–193.
47. Dominko, R.; Bele, M.; Goupil, J. M.; Gaberscek, M.; Hanzel, D.; Arcon, I.; Jamnik, J. Wired Porous Cathode Materials: A Novel Concept for Synthesis of $\mathrm{LiFePO_4}$. *Chem. Mater.* **2007**, *19*, 2960–2969.
48. Ellis, B. L.; Makahnouk, W. R. M.; Makimura, Y.; Toghill, K.; Nazar, L. F. A Multifunctional 3.5 V Iron-Based Phosphate Cathode for Rechargeable Batteries. *Nat. Mater.* **2007**, *6*, 749–753.
49. Xie, H. M.; Wang, R. S.; Ying, J. R.; Zhang, L. Y.; Jalbout, A. F.; Yu, H. Y.; Yang, G. L.; Pan, X. M.; Su, Z. M. Optimized $\mathrm{LiFePO_4}$-Polyacene Cathode Material for Lithium-Ion Batteries. *Adv. Mater.* **2006**, *18*, 2609–2613.
50. Yamada, A.; Hosoya, M.; Chung, S.-C.; Kudo, Y.; Hinokuma, K.; Liu, K. Y.; Nishi, Y. Olivine-type Cathodes: Achievements and Problems. *J. Power Sources* **2003**, *119*, 232–238.
51. Dominko, R.; Bele, M.; Gaberscek, M.; Remskar, M.; Hanzel, D.; Goupil, J. M.; Pejovnik, S.; Jamnik, J. Porous Olivine Composites Synthesized by Sol-gel Technique. *J. Power Sources* **2006**, *153*, 274–280.
52. Wang, Y. G.; Wang, Y. R.; Hosono, E.; Wang, K. X.; Zhou, H. S. The Design of a $\mathrm{LiFePO_4}$/Carbon Nanocomposite with a Core-Shell Structure and Its Synthesis by an *In Situ* Polymerization Restriction Method. *Angew. Chem., Int. Ed.* **2008**, *47*, 7461–7465.
53. Podsiadlo, P.; Kaushik, A. K.; Arruda, E. M.; Waas, A. M.; Shim, B. S.; Xu, J.; Nandivada, H.; Pumplin, B. G.; Lahann, J.;

Ramamoorthy, A.; Kotov, N. A. Ultrastrong and Stiff Layered Polymer Nanocomposites. *Science* **2007**, *318*, 80–83.

54. Shim, B. S.; Zhu, J.; Jan, E.; Critchley, K.; Kotov, N. A. Transparent Conductors from Layer-by-Layer Assembled SWNT Films: Importance of Mechanical Properties and a New Figure of Merit. *ACS Nano* **2010**, *4* (7), 3725–3734.
55. Zhu, J.; Shim, B. S.; Prima, M. D.; Kotov, N. A. Transparent Conductors from Carbon Nanotubes LBL-Assembled with Polymer Dopant with π-π Electron Transfer. *J. Am. Chem. Soc.* **2011**, *133* (19), 7450–7460.
56. Chen, Y.; Zhang, X.; Yu, P.; Ma, Y. W. Stable Dispersions of Graphene and Highly Conducting Graphene Films: A New Approach to Creating Colloids of Graphene Monolayers. *Chem. Commun.* **2009**, 4527–4529.
57. Xu, C. H.; Sun, J.; Gao, L. Synthesis of Novel Hierarchical Graphene/Polypyrrole Nanosheet Composites and Their Superior Electrochemical Performance. *J. Mater. Chem.* **2011**, *21*, 11253–11258.
58. Andres, C. M.; Fox, M. L.; Kotov, N. A. Traversing Material Scales: Macroscale LBL-Assembled Nanocomposites with Microscale Inverted Colloidal Crystal Architecture. *Chem. Mater.* **2012**, *24* (1), 9–11.
59. Andres, C.M.; Larraza, I.; Corrales, T.; Kotov, N.A. Nanocomposite Microcontainers. *Adv. Mater.* **2012**, *24*, 4597–4600.
60. Shao, L.; Jeon, J. W.; Lutkenhaus, J. L. Polyaniline/Vanadium Pentoxide Layer-by-Layer Electrodes for Energy Storage. *Chem. Mater.* **2012**, *24*, 181–189.
61. Andres, C. M.; Larraza, I.; Corrales, T.; Kotov, N. A. Nanocomposite Microcontainers. *Adv. Mater.* **2012**, *24*, 4597–4600.
62. Mai, L. Q.; Dong, Fei.; Xu, X.; Luo, Y. Z.; An, Q. Y.; Zhao, Y. L.; Pan, J.; Yang, J. N. Cucumber-Like V_2O_5/poly(3,4-ethylenedioxythiophene) & MnO_2 Nanowires with Enhanced Electrochemical Cyclability. *Nano Lett.* **2013**, *13*, 740–745.
63. Zhu, J.; Andres, C. M.; Xu, J.; Ramamoorthy, A.; Tsotsis, T.; Kotov, N. A. Pseudonegative Thermal Expansion and the State of Water in Graphene Oxide Layered Assemblies. *ACS Nano* **2012**, *6*, 8357–8365.
64. Lee, J. K.; Smith, K. B.; Hayner, C. M.; Kung, H. H. Silicon Nanoparticles-Graphene Paper Composites for Li Ion Battery Anodes. *Chem. Commun.* **2010**, *46*, 2025–2027.
65. Wang, J. Z.; Zhong, C.; Chou, S. L.; Liu, H. K. Flexible Free-Standing Graphene-Silicon Composite Film for Lithium-Ion Batteries. *Electrochem. Commun.* **2010**, *12*, 1467–1470.
66. Wu, C.; Huang, X. Y.; Wang, G. L.; Lv, L. B.; Chen, G.; Li, G. Y.; Jiang, P. K. Highly Conductive Nanocomposites with Three-Dimensional, Compactly Interconnected Graphene Networks *via* a Self-Assembly Process. *Adv. Funct. Mater.* **2013**, *23*, 506–513.
67. Stankovich, S.; Dikin, D. A.; Dommett, G. H. B.; Kohlhaas, K. M.; Zimney, E. J.; Stach, E. A.; Piner, R. D.; Nguyen, S. T.; Ruoff, R. S. Graphene-Based Composite Materials. *Nature* **2006**, *442*, 282–286.
68. Lee, D. W.; Hong, T. K.; Kang, D. W.; Lee, J. S.; Heo, M. H.; Kim, J. Y.; Kim, B. S.; Shin, H. S. Highly Controllable Transparent and Conducting Thin Films using Layer-by-Layer Assembly of Oppositely Charged Reduced Graphene Oxides. *J. Mater. Chem.* **2011**, *21*, 3438–3442.
69. Wang, G. X.; Shen, X. P.; Yao, J.; Park, J. Graphene Nanosheets for Enhanced Lithium Storage in Lithium Ion Batteries. *Carbon* **2009**, *47*, 2049–2053.
70. Ferrari, A. C.; Robertson, J. Interpretation of Raman Spectra of Disordered and Amorphous Carbon. *Phys. Rev. B* **2000**, *61*, 14095–14107.
71. Stankovich, S.; Dikin, D. A.; Piner, R. D.; Kohlhaas, K. A.; Kleinhammes, A.; Jia, Y.; Wu, Y.; Nguyen, S. B. T.; Ruoff, R. S. Synthesis of Graphene-Based Nanosheets *via* Chemical Reduction of Exfoliated Graphite Oxide. *Carbon* **2007**, *45*, 1558–1565.
72. Tang, Z. Y.; Kotov, N. A.; Magonov, S.; Ozturk, B. Nanostructured Artificial Nacre. *Nat. Mater.* **2003**, *2*, 413–418.
73. Whitehead, A. H.; Schreiber, M. Current Collectors for Positive Electrodes of Lithium-Based Batteries. *J. Electrochem. Soc.* **2005**, *152*, A2105–A2113.
74. Tung, S. O.; Ho, S.; Yang, M.; Zhang, R. L.; Kotov, N. A. A Dendrite-Suppressing Solid Ion Conductor From Aramid Nanofibers. *Nat. Commun.* **2015**, *6*, 6152–6158.
75. Liu, L.; Choi, B. G.; Tung, S. O.; Hu, T.; Liu, Y.; Li, T; Zhao, T.; Kotov, N. A. Low-Current Field-Assisted Assembly of Copper Nanoparticles for Current Collectors, *Faraday Disc.* **2015,** C4FD00263F, in press.